

<sup>1</sup> **Effect of local host density and size on forest insect severity depends  
2 on climatic water deficit**

<sup>3</sup> Michael J. Koontz<sup>1,2,\*</sup>, Andrew M. Latimer<sup>1,2</sup>, Leif A. Mortenson<sup>3</sup>, Christopher J. Fettig<sup>3</sup>, Malcolm P.  
<sup>4</sup> North<sup>1,2,4</sup>

<sup>5</sup> <sup>1</sup>Graduate Group in Ecology, University of California, Davis, CA, USA

<sup>6</sup> <sup>2</sup>Department of Plant Sciences, University of California, Davis, CA, USA

<sup>7</sup> <sup>3</sup>USDA Forest Service, Pacific Southwest Research Station, Placerville, CA, USA

<sup>8</sup> <sup>4</sup>USDA Forest Service, Pacific Southwest Research Station, Davis, CA, USA

<sup>9</sup> \*Correspondence: michael.koontz@colorado.edu

<sup>10</sup> Date report generated: April 05, 2019

<sup>11</sup> **Abstract**

<sup>12</sup> Bark beetles are a primary mortality agent of trees in western U.S. forests, and the recent Californian hot  
<sup>13</sup> drought of 2012 to 2015 created favorable conditions for bark beetle-induced tree mortality throughout the  
<sup>14</sup> yellow pine/mixed-conifer forest system in the Sierra Nevada mountain range. The western pine beetle,  
<sup>15</sup> *Dendroctonus brevicomis*, is the forest insect that is largely responsible for the especially common deaths of its  
<sup>16</sup> main host in California, the ponderosa pine tree (*Pinus ponderosa*). While previous work has demonstrated a  
<sup>17</sup> link between climate conditions related to tree water stress and forest density on the severity of the western  
<sup>18</sup> pine beetle disturbance, it remains challenging to disentangle the relative effects of these variables. Further,  
<sup>19</sup> forest density can affect western pine beetle behavior in a number of ways, which creates a need for more  
<sup>20</sup> information on complex forest structure (including local density, tree size, and the heterogeneity of these  
<sup>21</sup> variables across a forest stand) to uncover the most likely mechanism.

<sup>22</sup> We conducted aerial surveys over an established network of 32 permanent vegetation monitoring plots along  
<sup>23</sup> a 350km and 1000m elevation gradient in the Sierra Nevada mountain range of California using a small,  
<sup>24</sup> unhumanned aerial system (sUAS aka drone) equipped with a narrow-band multispectral camera. Using  
<sup>25</sup> Structure from Motion (SfM) processing on over 450,000 images, we reconstructed the complex vegetation  
<sup>26</sup> structure of over 9 square kilometers of forest that experienced ponderosa pine mortality as a result of  
<sup>27</sup> western pine beetle activity. Using this dataset, we built a model to predict the probability of ponderosa  
<sup>28</sup> pine mortality as a function of forest structure variables (including ponderosa pine density and mean size, as  
<sup>29</sup> well as all tree density and mean size), an environmental gradient of climatic water deficit, and a Gaussian

30 process to capture spatial covariance in the response.

31 Data from small, unhummaned aerial systems (sUAS) can provide important context surrounding ground  
32 plots, which enables inference and generates new insights into ecological processes. sUAS are best-suited to  
33 enhancing ground data, which implies that we need not abandon lessons learned from sound experimental  
34 design (i.e., a network of plots along a gradient is still a powerful way to use sUAS data).

35 Host availability for aggressive bark beetles appears to have played the dominant role in increasing the  
36 probability of ponderosa pine mortality in the most hard-hit forest stands during the cumulative mortality  
37 event of 2012 to 2018. Host size played a role in its interaction with environmental condition– climatic  
38 water deficit– such that numerous and smaller host trees increased the probability of ponderosa mortality at  
39 cool/wet sites, while numerous and larger host trees increased the probability of ponderosa mortality at  
40 hot/dry sites.

41 Our results corroborate the role of host tree density and regional climate conditions on the severity of forest  
42 insect disturbance, but also highlight the importance of complex forest structure (i.e., both host density and  
43 average host size) in its interaction with regional climate. Thus, the future forest structure may be affected  
44 differently by a large-scale forest insect disturbance for the same host tree/forest insect pairing, and during  
45 the same extreme drought, but across a gradient of regional climate conditions.

## 46 Introduction

47 Aggressive bark beetles dealt the final blow to many of the nearly 150 million trees killed in the California  
48 drought of 2012 to 2015 and its aftermath (USDAFS 2019). A harbinger of climate change effects to come,  
49 high temperatures exacerbating the extreme drought led to tree mortality events of unprecedented size in the  
50 driest, densest forests across the state (Millar and Stephenson 2015, Young et al. 2017). A century of fire  
51 suppression policy has enabled forests to grow into dense stands, which increases water stress on trees and  
52 makes them more vulnerable to bark beetle attack (Fettig 2012, North et al. 2015).

53 Forests in California’s Sierra Nevada region are characterized by regular bark beetle disturbances that interact  
54 with forest structure. Bark beetles shape forest structure as they sporadically kill weakened trees under  
55 normal conditions, or wide swaths of even healthy trees under outbreak conditions (Raffa et al. 2015). Forest  
56 structure also strongly influences bark beetle activity. Low-density forests are less prone to bark beetle  
57 attacks (Fettig 2012), but resolving the mechanism underlying this observation requires a more nuanced view  
58 of forest structure. For instance, a low-density forest may resist attack because longer dispersal distances are  
59 required for successful colonization of new hosts, because widely-spaced trees experience less competition

60 for water resources and thus average tree vigor is greater (Hayes et al. 2009), or because its wider canopy  
61 openings disrupt pheromone signaling between beetles (Fettig 2012).

62 Tree density is often a coarse gauge of the size and spatial distribution of trees— the forest structure— with  
63 which bark beetles interact (Raffa et al. 2008). Climate change mitigation strategies emphasize reducing tree  
64 densities (North et al. 2015, Young et al. 2017), but understanding the optimal scale and pattern of tree  
65 distribution that can mitigate bark beetle outbreaks will be vital for predicting how California forests may  
66 respond to these interventions. Recent research has shown a strong link between complex forest structure  
67 and forest resilience, but measuring this complexity generally requires expensive equipment or labor-intensive  
68 field surveys (Larson and Churchill 2012, Kane et al. 2014). These barriers restrict survey frequency and  
69 extent, which limits insights into phenomena like bark beetle outbreaks that rapidly emerge over weeks to  
70 months but have long-lasting effects on forest conditions. Further, the vast spatial extent and environmental  
71 gradient of mortality (Young et al. 2017, USDAFS 2019) challenges our ability to simultaneously consider  
72 how environmental conditions may interact with local forest structure to produce patterns of insect activity.  
73 Small, unhumanned aerial systems (sUAS) enable fast and relatively cheap remote imaging over dozens of  
74 hectares of forest, which can be used to determine both forest structure and tree condition at the individual  
75 tree scale (Morris et al. 2017, Shiklomanov et al. 2019).

76 We used ultra-high resolution remote sensing data from a small, unhumanned aerial system over a network of  
77 32 sites in the Sierra Nevada spanning 1000m of elevation and 350km of latitude and covering a total of 9  
78 square kilometers of forest to ask how fine-scale forest structure affected the probability of tree mortality  
79 during the cumulative mortality event of 2012 to 2018. We asked:

- 80 1. How does local host tree density and size affect the severity of western pine beetle disturbance?
- 81 2. How does total tree density and size affect the severity of western pine beetle disturbance?
- 82 3. How does environmentally-driven tree moisture stress affect the severity of western pine beetle distur-  
83 bance?
- 84 4. Do the effects of forest structure and environmental condition on western pine beetle disturbance  
85 interact?

86 Which trees die during drought? Gradient of stress to host selection. Stephenson et al. (2019) argue that  
87 there are differences across species during an extreme drought on whether environment or forest structure  
88 drives mortality. But even within the same species, there could be *interaction* between the background  
89 environmental condition and the forest struture in driving mortality that gives rise to stress-dominated

90 mortality in some locations and host-selection dominated mortality in other locations *for the same species*.

91 **Methods**

92 **Study system**

93 The study sites comprise mostly ponderosa pine trees, *Pinus ponderosa*, whose primary bark beetle predator  
94 in California is the western pine beetle (WPB), *Dendroctonus brevicomis*. The WPB is an aggressive bark  
95 beetle, meaning it must attack and kill live trees in order to successfully reproduce (Raffa et al. 2008).  
96 Pioneer WPBs disperse to a new host tree, determine the host's susceptibility to attack, and use pheromone  
97 signals to attract other WPBs. The attracted WPBs mass attack the tree by boring into its inner bark,  
98 laying eggs, and dying, leaving their offspring to develop inside the doomed tree before themselves dispersing  
99 (Raffa et al. 2008). Small WPB populations prefer weakened trees but large populations can overwhelm  
100 the defense mechanisms of even healthy trees. Successful attacks on large, healthy trees are boons to bark  
101 beetle fecundity and trigger outbreaks in which populations explode and massive tree mortality occurs. In  
102 California, the WPB can have 3 generations in a single year giving it a greater potential to spread rapidly  
103 through forests than its more infamous congener, the mountain pine beetle, *Dendroctonus ponderosa* (MPB).

104 We built our study on 180 vegetation/forest insect monitoring plots at 36 sites established between 2016 and  
105 2017 (Fettig et al. 2019). These established plots were located in beetle-attacked, mixed-conifer forests across  
106 the Eldorado, Stanislaus, Sierra and Sequoia National Forests and were stratified by elevation (914-1219  
107 meters [3000-4000 feet], 1219-1524 meters [4000-5000 feet], 1524-1828 meters [5000-6000 feet] above sea level).  
108 In the Sequoia National Forest, the National Forest that is furthest south, plots were stratified with the lowest  
109 elevation band between 1219 and 1524 (4000-5000 feet) and extended to an upper elevation band of 1828-2133  
110 (6000-7000 feet) to capture a more similar forest community composition as at the more northern National  
111 Forests. The sites have variable forest structure and disturbance history and plot locations were selected  
112 specifically in areas with >40% ponderosa pine basal area and >10% ponderosa pine mortality. The 0.04ha  
113 circular plots are clustered along transects in groups of 5, with between 80 and 200m between each plot. All  
114 trees within the plot were assessed as dead or alive. The stem location of all trees was mapped relative to the  
115 center of each plot using azimuth/distance measurements. Tree identity to species and diameter at breast  
116 height (dbh) were recorded if dbh was greater than 6.35cm. During the spring and early summer of 2018, all  
117 field plots were revisited to assess whether dead trees had fallen (Fettig et al. 2019).

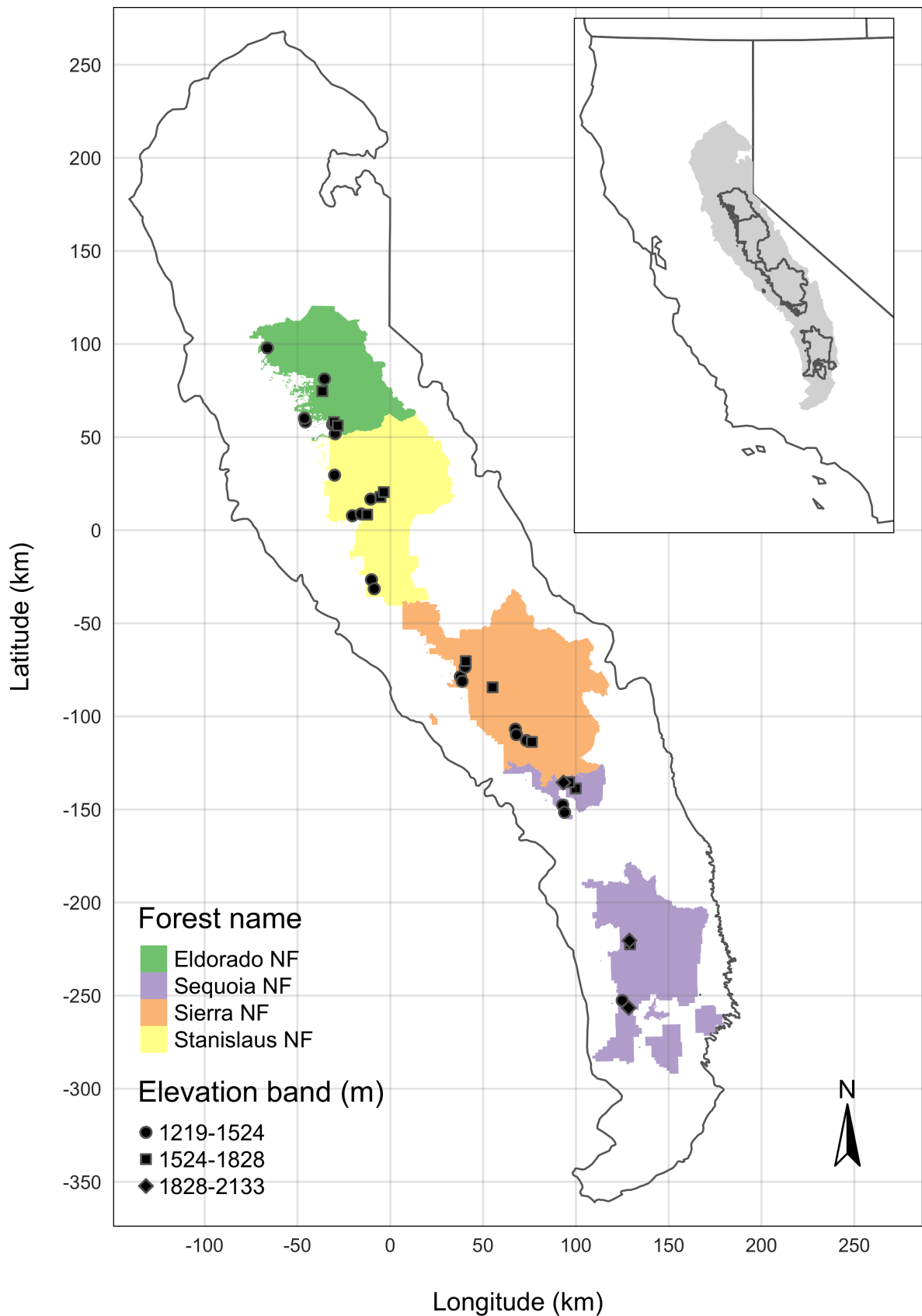


Figure 1: Geographic extent of the study.  
5

118 **Instrumentation**

119 Imagery was captured using a DJI Zenmuse X3 RGB camera (DJI 2015a) and a Micasense RedEdge3 5-band  
120 multispectral camera (Micasense 2015). We mounted both of these instruments simultaneously on a DJI  
121 Matrice 100 aircraft (DJI 2015b) using the DJI 3-axis stabilized gimbal for the Zenmuse X3 camera and a  
122 Micasense angled fixed mount for the RedEdge3 camera. The gimbal and the angled fixed mount ensured  
123 both instruments were nadir-facing during image capture. Just prior or after image capture at each site, we  
124 calibrated the RedEdge3 camera by taking an image of a calibration panel on the ground in full sun with  
125 known reflectance values for each of the 5 narrow bands.

Table 1: Reflectance sensitivity of the Micasense Rededge3 camera. The calibration panel value represents the reflectance of the calibration panel for the given wavelength.

| Band number | Band name           | Center wavelength | Band width | Wavelength range | Panel reflectance |
|-------------|---------------------|-------------------|------------|------------------|-------------------|
| 1           | blue (b)            | 475               | 20         | 465-485          | 0.64              |
| 2           | green (g)           | 560               | 20         | 550-570          | 0.64              |
| 3           | red (r)             | 668               | 10         | 663-673          | 0.64              |
| 4           | near infrared (nir) | 840               | 40         | 820-860          | 0.60              |
| 5           | red edge (re)       | 717               | 10         | 712-722          | 0.63              |

126 **Flight protocol**

127 Image capture was conducted as close to solar noon as possible to minimize shadow effects (always within 4  
128 hours; usually within 2 hours). Prior to the aerial survey, two strips of bright orange drop cloth (~100cm x  
129 15cm) were positioned as an “X” over the permanent monuments marking the center of the 5 field plots from  
130 Fettig et al. (2019).

131 For each of the 36 sites (containing 5 plots each), we captured imagery over the surrounding ~40 hectares  
132 of forested area using north-south aerial transects. For XXXXX sites, we surveyed less surrounding area  
133 in order to maintain visual and radio communication with the aircraft during flight (Table XXXXXX; as a  
134 supplement, I think; Columns: Site, forest, elevation, rep, CWD, surveyed area, survey date).

135 We preprogrammed transect paths using Map Pilot for DJI on iOS (hereafter Map Pilot) (Easy 2018). All  
136 transects tracked the terrain and their altitude remained approximately constant at 120 meters above ground  
137 level in order to maintain consistent ground sampling distance in the imagery. Ground level was based on a

<sup>138</sup> 1-arc-second digital elevation model (Farr et al. 2007) and we implemented terrain following using Map Pilot.  
<sup>139</sup> For this analysis, we dropped 4 sites whose imagery was of insufficient quality to process.

<sup>140</sup> Structure from motion (SfM) processing requires highly overlapping images, especially in densely vegetated  
<sup>141</sup> areas. We planned transects with 90% forward overlap and 90% side overlap at 100 meters below the lens.  
<sup>142</sup> Thus, with flights being at 120 meters above ground level, we achieved slightly higher than 90/90 overlap for  
<sup>143</sup> objects 20 meters tall or shorter (91.6/91.6 overlap at the ground). Overlap values were based on focal length  
<sup>144</sup> (3.6mm), sensor width (6.2mm), and image dimension (4000x3000 pixels) parameters of the Zenmuse X3  
<sup>145</sup> camera. Images were captured at a constant rate of 1 image every 2 seconds for both cameras. A forward  
<sup>146</sup> overlap of 90% at 100 meters translates to a flight speed of approximately 6.45 m/s and a side overlap of 90%  
<sup>147</sup> at 100 meters translates to transects approximately 17.2 meters apart. The Rededge camera has a different  
<sup>148</sup> focal length (5.4mm), sensor width (4.8mm), and image dimension (1280x960 pixels), which translates to  
<sup>149</sup> image overlap of 80.7/80.7 at 100m below the lens and 83.9/83.9 at ground level. Approximately 1900 photos  
<sup>150</sup> were captured over each 40 hectare survey area for each camera.

### <sup>151</sup> **Structure from motion/Photogrammetric processing**

<sup>152</sup> We used structure from motion (SfM), aka photogrammetry, to generate orthorectified reflectance maps,  
<sup>153</sup> digital surface models, and dense point clouds for each field site. We used Pix4Dmapper Cloud to process  
<sup>154</sup> imagery using parameters ideal for images of a densely vegetated area taken by a multispectral camera.  
<sup>155</sup> For three sites, we processed the RGB and the multispectral imagery in the same project to enhance the  
<sup>156</sup> resolution of the dense point cloud. All SfM projects resulted in a single processing “block,” indicating that  
<sup>157</sup> all images in the project were optimized and processed together.

### <sup>158</sup> **Creating canopy height models**

<sup>159</sup> We classified each survey area’s dense point cloud into “ground” and “non-ground” points using a cloth  
<sup>160</sup> simulation filter algorithm (Zhang et al. 2016) implemented in the **lidR** (Roussel et al. 2019) package. We  
<sup>161</sup> rasterized the ground points using the **raster** package (Hijmans et al. 2019) to create a digital terrain model  
<sup>162</sup> representing the ground underneath the vegetation at 1 meter resolution. We created a canopy height model  
<sup>163</sup> by subtracting the digital terrain model from the digital surface model created in Pix4Dmapper.

### <sup>164</sup> **Tree detection**

<sup>165</sup> We tested a total of 7 automatic tree detection algorithms and a total of 177 parameter sets on the canopy  
<sup>166</sup> height model or the dense point cloud to locate trees within each site (Table XXXXX; algorithm, number of

parameter sets, reference). We used 3 parameter sets of a variable window filter implemented in `ForestTools` (Plowright 2018) including the default variable window filter function in `ForestTools` as well as the “pines” and “combined” functions from Popescu and Wynne (2004). We used 6 parameter sets of a local maximum filter implemented in `lidR`. We used 131 parameter sets of the algorithm from Li et al. (2012), which operates on the original point cloud. These parameter sets included those from Shin et al. (2018) and Jakubowski et al. (2013). We used 3 parameter sets of the `watershed` algorithm implemented in `lidR`, which is a wrapper for a function in the `EBImage` package (Pau et al. 2010). We used 3 parameter sets of `ptrees` (Vega et al. 2014) implemented in `lidR` (Roussel et al. 2019) and `lidRplugins` (Roussel 2019) and which operates on the raw point cloud, without first normalizing it to height above ground level (i.e.. subtracting the ground elevation from the dense point cloud). We used the default parameter set of the `multichm` (Eysn et al. 2015) algorithm implmented in `lidR` (Roussel et al. 2019) and `lidRplugins` (Roussel 2019). We used 30 parameter sets of the experimental algorithm `lmfx` (Roussel 2019).

## Map ground data

Each orthorectified reflectance map was inspected to locate the 5 orange “X”s marking the center of the field plots. We were able to locate 110 out of 180 field plots and were then able to use these plots for validation of automated tree detection algorithms. We used the `sf` package (Pebesma et al. 2019) to convert distance-from-center and azimuth measurements of each tree in the ground plots to an x-y position on the SfM-derived reflectance map using the x-y position of the orange X visible in the reflectance map as the center.

## Correspondence of automatic tree detection with ground data

We calculated 7 forest structure metrics for each field plot using the ground data collected by Fettig et al. (2019): total number of trees, number of trees greater than 15 meters, number of trees less than 15 meters, mean height of trees, 25<sup>th</sup> percentile tree height, 75<sup>th</sup> percentile tree height, mean distance to nearest tree neighbor, mean distance to 2<sup>nd</sup> nearest neighbor.

For each tree detection algorithm and parameter set described above, we calculated the same set of 7 structure metrics within the footprint of the validation field plots. We calculated the Pearson’s correlation and root mean square error (RMSE) between the ground data and the aerial data for each of the 7 structure metrics for each of the 177 automatic tree detection algorithms/parameter sets.

For each algorithm and parameter set, we calculated its performance relative to other algorithms as whether its Pearson’s correlation was within 5% of the highest Pearson’s correlation as well as whether its RMSE was

197 within 5% of the lowest RMSE. For each algorithm/parameter set, we summed the number of forest structure  
198 metrics for which it reached these 5% thresholds. For automatically detecting trees across the whole study,  
199 we selected the algorithm/parameter set that performed well across the most number of forest metrics.

200 **Segmentation of crowns**

201 We delineated individual tree crowns with a marker controlled watershed segmentation algorithm (Meyer and  
202 Beucher 1990) using the detected treetops as markers implemented in the `ForestTools` package (Plowright  
203 2018). If the automatic segmentation algorithm failed to generate a crown segment for a detected tree (e.g.,  
204 often snags with a very small crown footprint), a circular crown was generated with a radius of 0.5 meters. If  
205 the segmentation generated multiple polygons for a single detected tree, only the polygon containing the  
206 detected tree was retained. Image overlap decreases near the edges of the overall flight path, which reduces  
207 the quality of the SfM processing in those areas. Thus, we excluded segmented crowns within 35 meters of  
208 the edge of the survey area.

209 We used the `velox` package (Hunziker 2017) to extract all the pixel values from the orthorectified reflectance  
210 map for each of the 5 narrow bands within each segmented crown polygon. Per pixel, we additionally  
211 calculated the normalized difference vegetation index (NDVI; Rouse et al. (1973)), the normalized difference  
212 red edge (NDRE; Gitelson and Merzlyak (1994)), the red-green index (RGI; Coops et al. (2006)), the red  
213 edge chlorophyll index (CI[red edge]; Clevers and Gitelson (2013)), and the green chlorophyll index (CI[green];  
214 Clevers and Gitelson (2013)). For each crown polygon, we calculated the mean value for each raw and derived  
215 reflectance band (5 raw; 5 derived).

216 **Classification of trees**

217 We overlaid the segmented crowns on the reflectance maps from 20 sites spanning the latitudinal and  
218 elevational gradient in the study. Using QGIS, we hand classified XXXX trees as live/dead and as one  
219 of 5 dominant species in the study area (*Pinus ponderosa*, *Pinus lambertiana*, *Abies concolor*, *Calocedrus*  
220 *decurrens*, or *Quercus kelloggii*) using the mapped ground data as a guide.

221 We used all 10 mean values of the reflectance bands for each tree crown polygon to predict whether the hand  
222 classified trees were alive or dead using a boosted logistic regression model implemented in the `caret` package  
223 (Kuhn 2008). For just the living trees, we similarly used all 10 reflectance values to predict the tree species  
224 using regularized discriminant analysis implemented in the `caret` package, which proved to have the highest  
225 accuracy for a training dataset (accuracy = XXXXX, kappa = XXXXX).

226 Finally, we used these models to classify all tree crowns in the data set as alive or dead as well as the species

227 of living trees.

228 **Allometric scaling of height to basal area**

229 We converted the height of each tree determined using the canopy height model to its basal area. Using  
230 the tree height and diameter at breast height (DBH; breast height = 1.37m) ground data from Fettig et al.  
231 (2019), we fit a simple linear regression to predict DBH from height for each of the 5 dominant species. Using  
232 the model-classified tree species of each segmented tree, we used the corresponding linear relationship for  
233 that species to estimate the DBH given the tree's height. We then calculated each tree's basal area, assuming  
234 no tapering from breast height.

235 **Note on assumptions about dead trees**

236 For the purposes of this study, we assumed that all dead trees were ponderosa pine and were thus host trees.  
237 This is a reasonably good assumption, given that Fettig et al. (2019) found that 73.4% of the dead trees in  
238 the coincident ground plots were ponderosa pine.

239 **Rasterizing individual tree data**

240 Because the tree detection algorithms were validated against ground data at the plot level, we rasterized the  
241 classified trees at a spatial resolution similar to that of the ground plots (rasterized to 20m x 20m equalling  
242 400 m<sup>2</sup>; circular ground plots with 11.35m radius equalling 404 m<sup>2</sup>). In each raster cell, we tallied: number  
243 of alive trees, number of dead trees, number of ponderosa pine trees, number of non-ponderosa pine trees,  
244 basal area of ponderosa pine trees, basal area of non-ponderosa pine trees.

245 **Environmental data**

246 We used climatic water deficit (CWD) (Stephenson 1998) from the 1980-2010 mean value of the basin  
247 characterization model (Flint et al. 2013) as an integrated measure of temperature and moisture conditions  
248 for each cell. Higher values of CWD correspond to hotter, drier conditions and lower values correspond  
249 to cooler, wetter conditions CWD has been shown to correlate well with broad patterns of tree mortality  
250 in the Sierra Nevada (Young et al. 2017). We resampled the climatic water deficit product using bilinear  
251 interpolation implemented in the `raster` package to match the 20m x 20m spatial scale of the other variables.  
252 We converted the CWD value for each cell into a z-score representing that cell's deviation from the mean  
253 CWD across the climatic range of Sierra Nevada ponderosa pine as determined from XXXXX herbarium  
254 records described in Baldwin et al. (2017). Thus, a CWD z-score of one would indicate that the CWD at

255 that cell is one standard deviation hotter/drier than the mean CWD across all geolocated herbarium records  
 256 for ponderosa pine in the Sierra Nevada.

257 **Statistical model**

258 We used a generalized linear model with a zero-inflated binomial response and a logit link to predict the  
 259 probability of ponderosa pine mortality within each raster cell as a function of the crossed effects of ponderosa  
 260 pine quadratic mean diameter and density added to the crossed effect of overall quadratic mean diameter and  
 261 density as well as the interaction of each summand with climatic water deficit at each site.

262 To measure and account for spatial autocorrelation of the bark beetle behavioral processes underlying  
 263 ponderosa mortality, we first subsampled the data at each site to a random selection of 200, 20m x 20m  
 264 cells representing approximately 27.5% of the surveyed area. With these subsampled data, we included a  
 265 separate exact Gaussian process term per site of the interaction between the x- and y-position of each cell  
 266 using the `gp()` function in the `brms` package (Bürkner 2017). The Gaussian process accounts for spatial  
 267 autocorrelation in the model by jointly estimating the spatial covariance of the response variable with the  
 268 effects of the other covariates.

$$y_{i,j} \sim \begin{cases} 0, & p \\ Binom(n_i, \pi_i), & 1 - p \end{cases}$$

$$\begin{aligned} logit(\pi_i) = & \beta_0 + \\ & \beta_1 X_{cwd,j} + \\ & \beta_1 X_{cwd,j} (\beta_2 X_{\text{pip}oQMD,i} + \beta_3 X_{\text{pip}oDensity,i} + \beta_4 X_{\text{pip}oQMD,i} X_{\text{pip}oDensity,i}) + \\ & \beta_1 X_{cwd,j} (\beta_5 X_{\text{overall}QMD,i} + \beta_6 X_{\text{overall}Density,i} + \beta_7 X_{\text{overall}QMD,i} X_{\text{overall}Density,i}) + \\ & \mathcal{GP}_j(x_i, y_i) \end{aligned}$$

269 Where  $y_i$  is the number of dead trees in cell  $i$ ,  $n_i$  is the sum of the dead trees and live ponderosa pine trees  
 270 in cell  $i$ ,  $\pi_i$  is the probability of ponderosa pine tree mortality in cell  $i$ ,  $p$  is the probability of there being  
 271 zero dead trees in a cell arising as a result of an unmodeled process,  $X_{cwd,j}$  is the z-score of climatic water  
 272 deficit for site  $j$ ,  $X_{\text{pip}oQMD,i}$  is the scaled quadratic mean diameter of ponderosa pine in cell  $i$ ,  $X_{\text{pip}oDensity,i}$   
 273 is the scaled density of ponderosa pine trees in cell  $i$ ,  $X_{\text{overall}QMD,i}$  is the scaled quadratic mean diameter  
 274 of all trees in cell  $i$ ,  $X_{\text{overall}Density,i}$  is the scaled density of all trees in cell  $i$ ,  $x_i$  and  $y_i$  are the x- and y-  
 275 coordinates of the centroid of the cell in an EPSG3310 coordinate reference system, and  $\mathcal{GP}_j$  represents the

276 exact Gaussian process describing the spatial covariance between cells at site  $j$ .

277 We used 4 chains with 2000 iterations each (1000 warmup, 1000 samples), and confirmed chain convergence  
278 by ensuring all Rhat values were less than 1.1 (Brooks and Gelman 1998). We used posterior predictive  
279 checks to visually confirm model performance by overlaying the density curves of the predicted number of  
280 dead trees per cell over the observed number (Gabry et al. 2019). For the posterior predictive checks, we  
281 used 50 random samples from the model fit to generate 50 density curves and ensured curves were centered  
282 on the observed distribution, paying special attention to model performance at capturing counts of zero.

### 283 Software and data availability

284 All data are available via the Open Science Framework. Statistical analyses were performed using the **brms**  
285 packages. With the exception of the SfM software (Pix4Dmapper Cloud) and the GIS software QGIS, all  
286 data carpentry and analyses were performed using R (R Core Team 2018).

## 287 Results

Table 2: Site characteristics for each of the 32 sites. The site name consists of the forest name, elevation band, and rep separated by an underscore. The Eldorado National Forest is ‘elido’, the Stanislaus National Forest is ‘stan’, the Sierra National Forest is ‘sier’, and the Sequoia National Forest is ‘sequ’. The elevation band represents the lower bounds of the 305 meter (1000 foot) elevation bands in feet. Thus ‘3k’ implies that site was located between 3,000 and 4,000 feet (914-1219 meters). Aerially detected mortality and density of the whole site is presented along with the mortality and density calculated from the ground data (aerial / ground). The density is measured in trees per hectare (tpha).

| Site       | CWD (mm) | CWD (z-score) | Survey area (ha) | Mortality (aerial/ground) | Density (tpha; aerial/ground) |
|------------|----------|---------------|------------------|---------------------------|-------------------------------|
| elido_3k_1 | 678.45   | 0.32          | 31.02            | 0.11/0.61                 | 630.01/410.19                 |
| elido_3k_2 | 706.48   | 0.50          | 30.61            | 0.12/0.36                 | 444.26/647.42                 |
| elido_3k_3 | 654.51   | 0.16          | 30.95            | 0.22/0.36                 | 492.63/410.19                 |
| elido_4k_1 | 570.43   | -0.38         | 28.04            | 0.09/0.39                 | 632.82/588.11                 |
| elido_4k_2 | 642.20   | 0.08          | 28.41            | 0.15/0.78                 | 338.20/271.82                 |

| Site      | CWD (mm) | CWD (z-score) | Survey area (ha) | Mortality (aerial/ground) | Density (tpha; aerial/ground) |
|-----------|----------|---------------|------------------|---------------------------|-------------------------------|
| eldo_5k_1 | 663.09   | 0.22          | 28.44            | 0.11/0.44                 | 661.80/543.63                 |
| eldo_5k_2 | 627.38   | -0.01         | 30.02            | 0.12/0.36                 | 584.89/968.65                 |
| eldo_5k_3 | 598.66   | -0.20         | 29.73            | 0.07/0.32                 | 488.66/622.71                 |
| stan_3k_1 | 638.49   | 0.06          | 31.04            | 0.10/0.52                 | 739.45/1037.84                |
| stan_3k_2 | 739.23   | 0.71          | 18.78            | 0.40/0.78                 | 433.53/405.25                 |
| stan_3k_3 | 761.64   | 0.86          | 30.10            | 0.22/0.41                 | 558.43/326.18                 |
| stan_4k_1 | 540.16   | -0.58         | 29.62            | 0.29/0.63                 | 507.61/711.66                 |
| stan_4k_2 | 528.07   | -0.66         | 30.54            | 0.18/0.56                 | 481.85/256.99                 |
| stan_5k_1 | 523.51   | -0.69         | 30.94            | 0.19/0.54                 | 388.89/336.06                 |
| stan_5k_2 | 523.95   | -0.68         | 29.94            | 0.21/0.44                 | 399.33/622.71                 |
| sier_3k_1 | 763.54   | 0.87          | 30.42            | 0.19/0.48                 | 651.46/850.04                 |
| sier_3k_2 | 767.64   | 0.90          | 30.05            | 0.20/0.77                 | 438.84/153.21                 |
| sier_3k_3 | 772.98   | 0.93          | 29.77            | 0.32/0.77                 | 511.26/459.62                 |
| sier_4k_1 | 841.25   | 1.38          | 30.43            | 0.54/0.51                 | 576.15/538.69                 |
| sier_4k_2 | 764.38   | 0.88          | 29.30            | 0.33/0.57                 | 499.43/854.98                 |
| sier_4k_3 | 688.34   | 0.38          | 26.39            | 0.48/0.59                 | 454.23/499.15                 |
| sier_5k_1 | 721.59   | 0.60          | 14.59            | 0.41/0.43                 | 631.30/716.60                 |
| sier_5k_2 | 709.96   | 0.52          | 27.53            | 0.53/0.74                 | 477.29/454.67                 |
| sier_5k_3 | 778.53   | 0.97          | 28.93            | 0.33/0.43                 | 569.44/484.33                 |
| sequ_4k_1 | 766.61   | 0.89          | 29.59            | 0.50/0.56                 | 365.81/607.88                 |
| sequ_4k_3 | 815.60   | 1.21          | 29.69            | 0.35/0.71                 | 433.35/306.41                 |
| sequ_5k_1 | 718.24   | 0.58          | 27.12            | 0.35/0.52                 | 364.01/444.79                 |
| sequ_5k_2 | 587.26   | -0.27         | 29.10            | 0.45/0.43                 | 478.31/499.15                 |
| sequ_5k_3 | 611.33   | -0.12         | 31.34            | 0.42/0.48                 | 348.68/494.21                 |
| sequ_6k_1 | 730.52   | 0.66          | 27.78            | 0.30/0.70                 | 433.43/360.77                 |
| sequ_6k_2 | 689.51   | 0.39          | 11.83            | 0.26/0.43                 | 699.04/934.06                 |
| sequ_6k_3 | 602.65   | -0.17         | 26.51            | 0.36/0.32                 | 535.54/691.89                 |

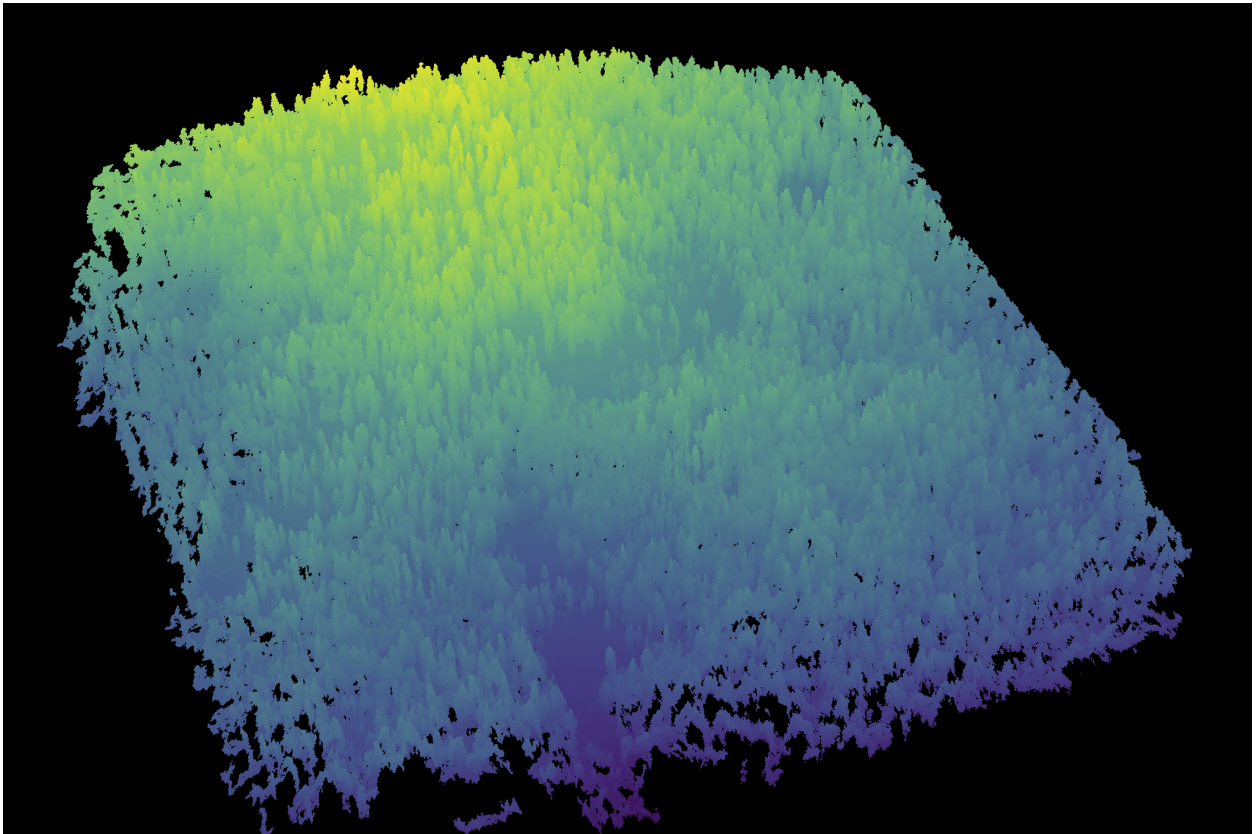


Figure 2: A dense point cloud representing ~40 hectares of forest is generated using Structure from Motion (SfM) processing of ~1900 images. The dense point cloud z- position represents the ground elevation plus the vegetation height.

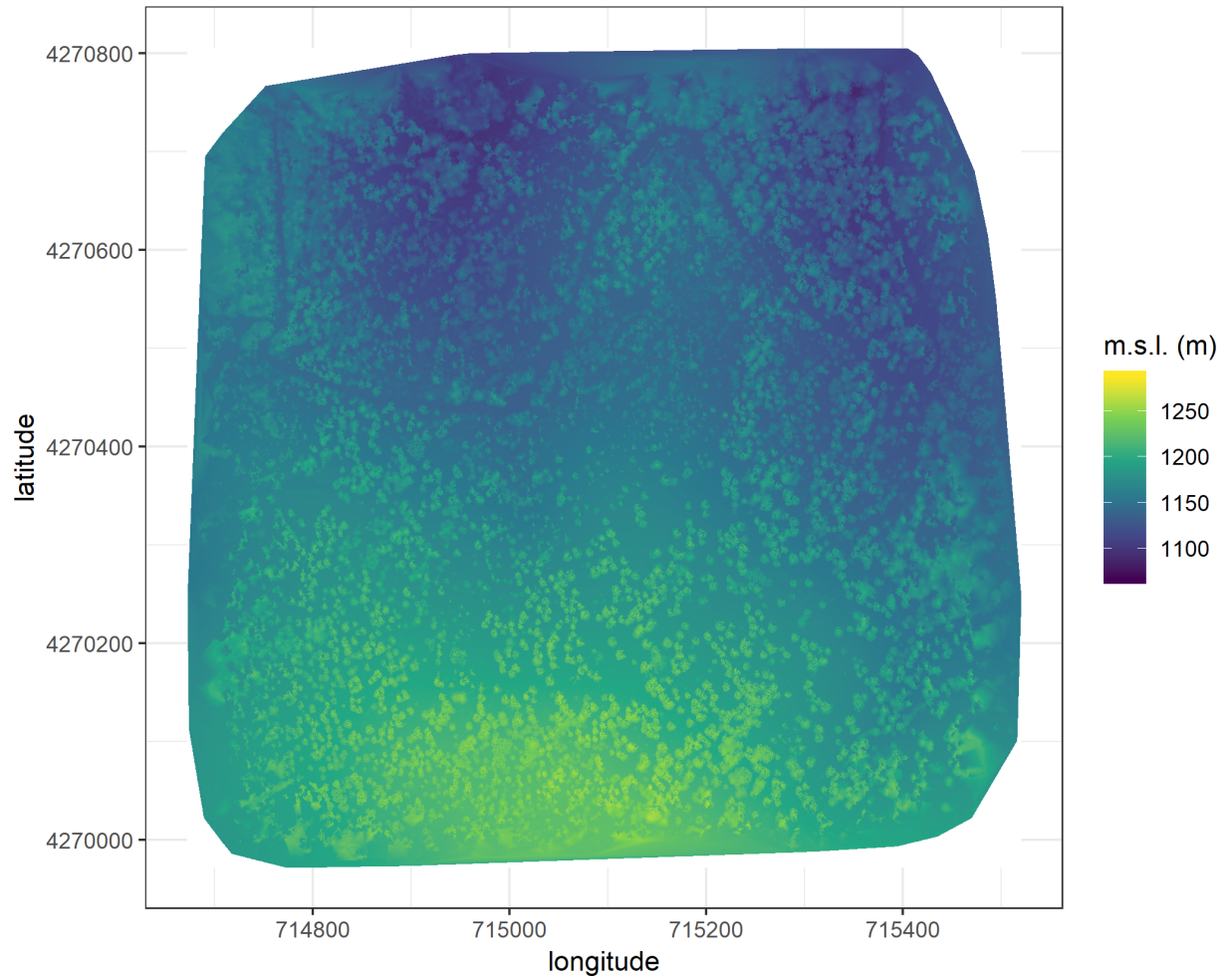


Figure 3: The digital surface model (DSM) is a 2-dimensional representation of the dense point cloud generated using structure from motion (SfM) processing. The DSM represents the ground elevation plus the vegetation height.

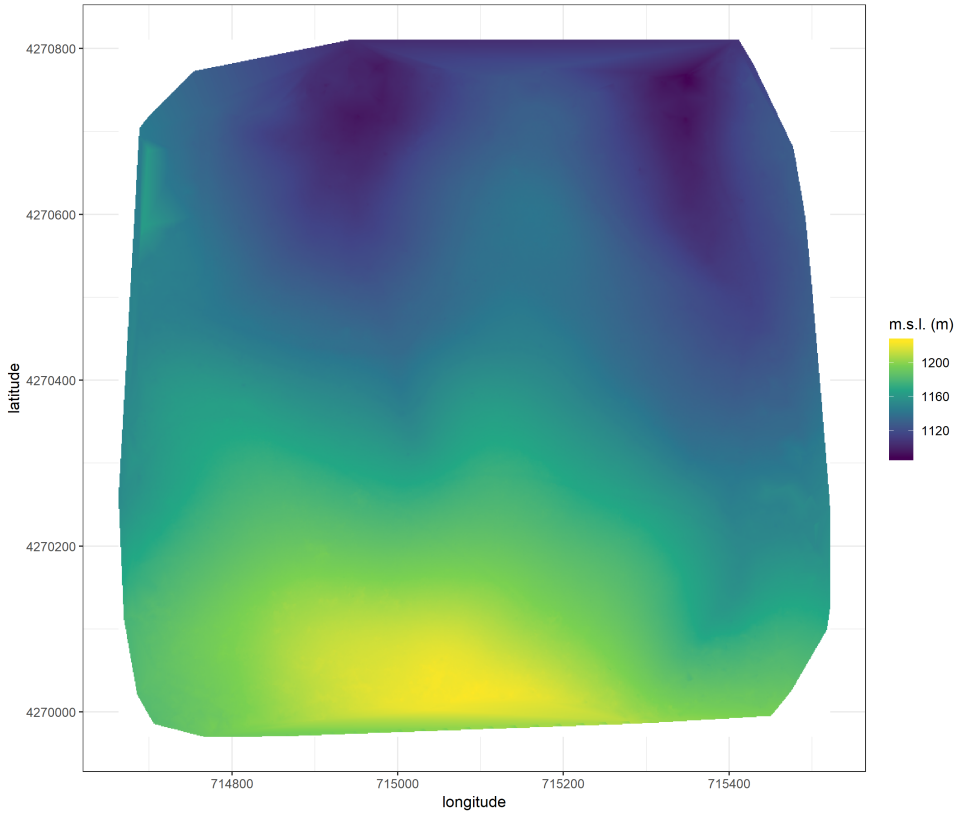


Figure 4: The digital terrain model (DTM) is generated by processing the dense point cloud using the cloth simulation filter algorithm (Zhang et al. 2016), which classifies points as “ground” or “not-ground” and then interpolates the “ground” elevation using Delaunay triangulation for the rest of the dense point cloud footprint. The DTM represents the ground elevation without any vegetation.

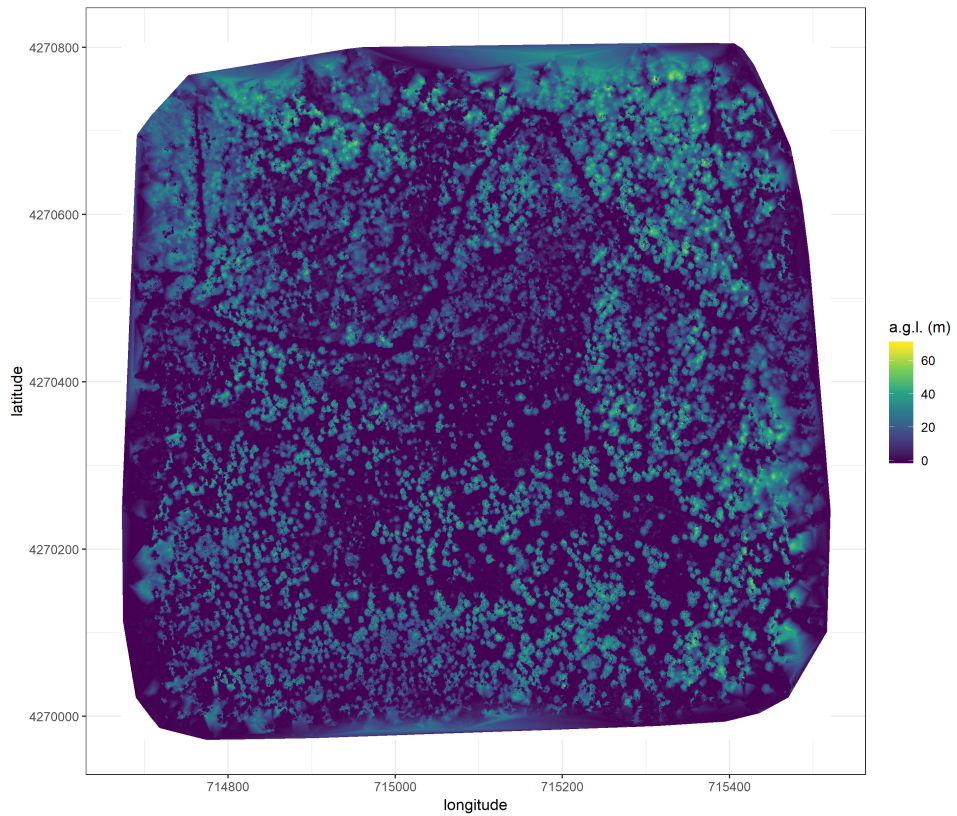


Figure 5: The canopy height model (CHM) is generated by subtracting the digital terrain model from the digital surface model. The CHM represents the height of all of the elevation above ground level.

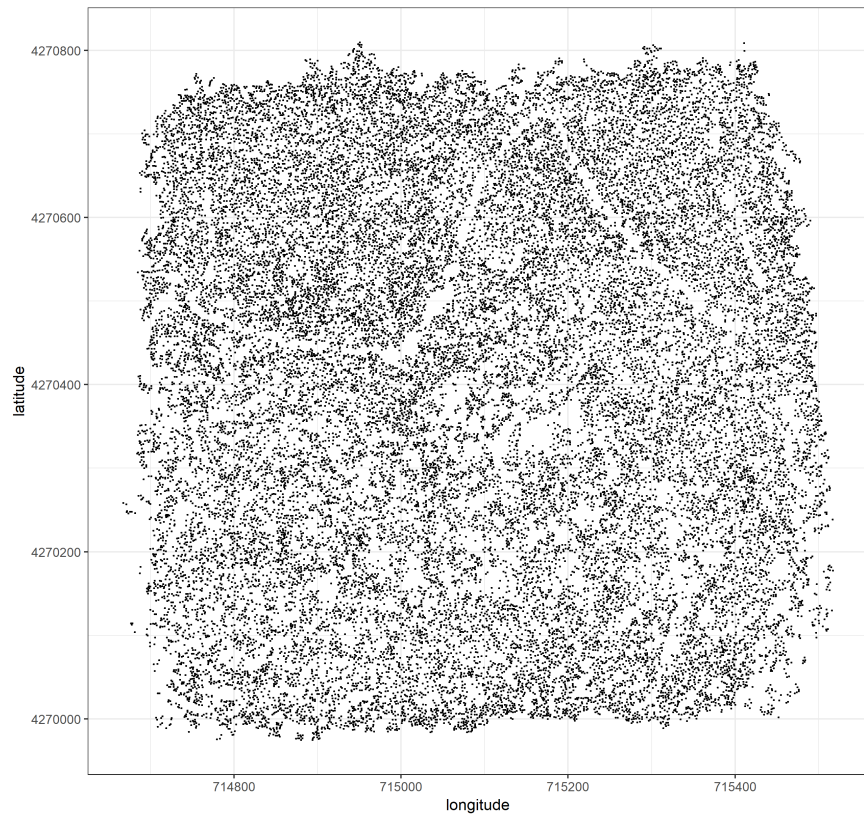


Figure 6: Tree locations are detected using the `lmfx` (Roussel et al. 2019) treetop detection algorithm on the dense point cloud.

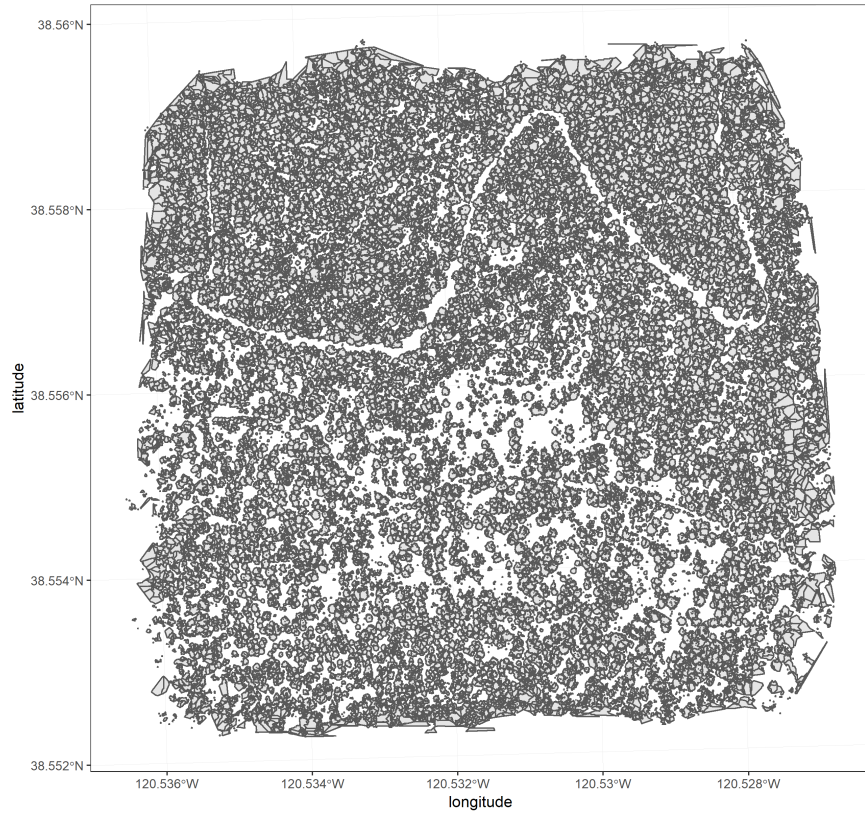


Figure 7: Individual crowns are delineated using a marker controlled watershed segmentation algorithm (Meyer and Beucher 1990, Plowright 2018) on the canopy height model (CHM) using the detected tree locations as a priority map. If the algorithm failed to delineate a crown for a tree that was identified in the tree detection step, a circular crown with a 0.5m buffer centered on point location of the detected tree was added as a crown. The crowns of snags were sometimes too small to be properly delineated, and the manually-created circular buffer

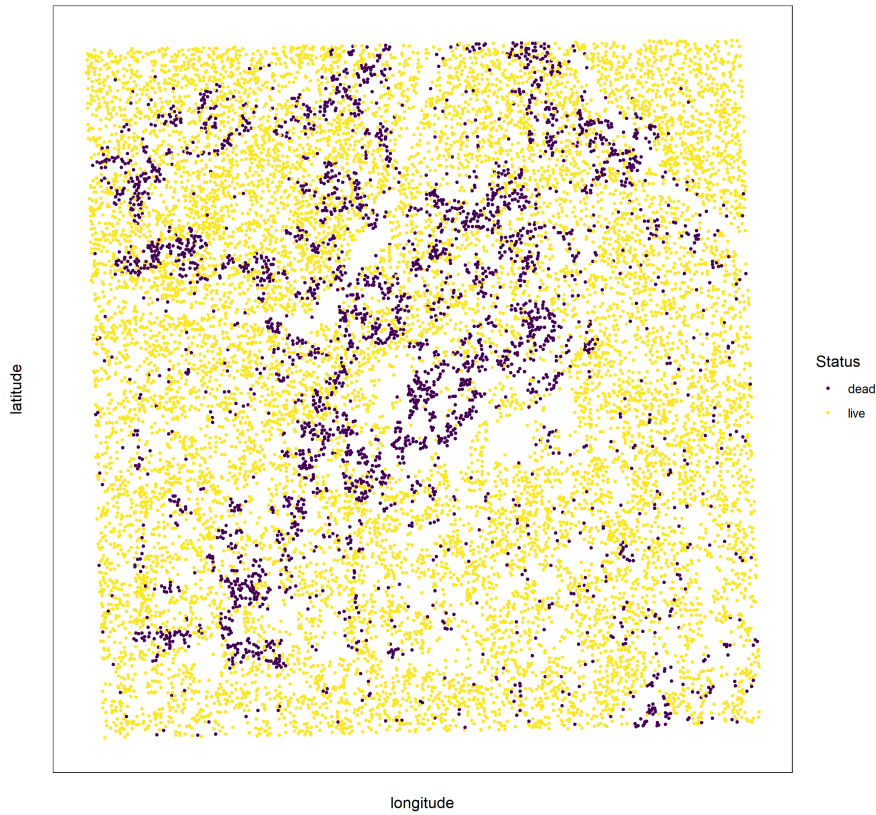


Figure 8: Each tree is classified as live or dead by extracting the pixel values from the 5 narrow bands of the Rededge3 camera (and 5 derived bands—see methods) in the orthomosaic within each segmented tree crown of the detected trees, taking their mean value, and using those means to predict live/dead status with a boosted logistic regression previously trained on a hand-classified set of segmented crowns from across the study area.

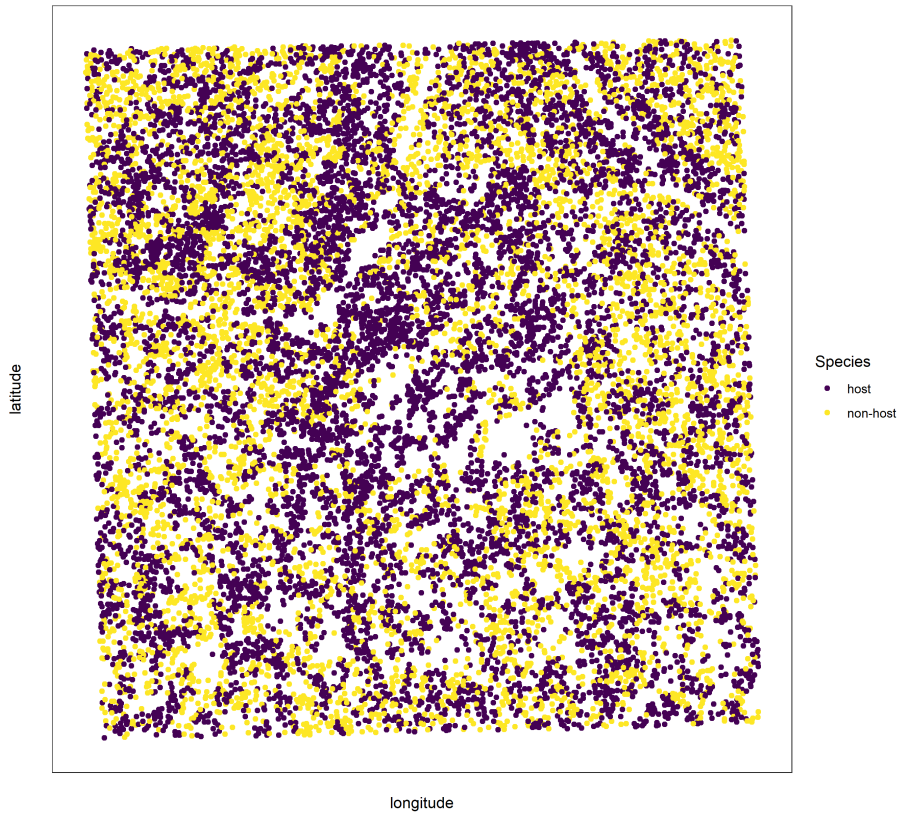


Figure 9: For each live tree, we classified its species using the same means of extracted pixel values across the 5 Rededge3 narrow bands (and 5 derived bands) as predictors in a regularized discriminant analysis previously trained on a hand-classified set of segmented crowns from across the study area.

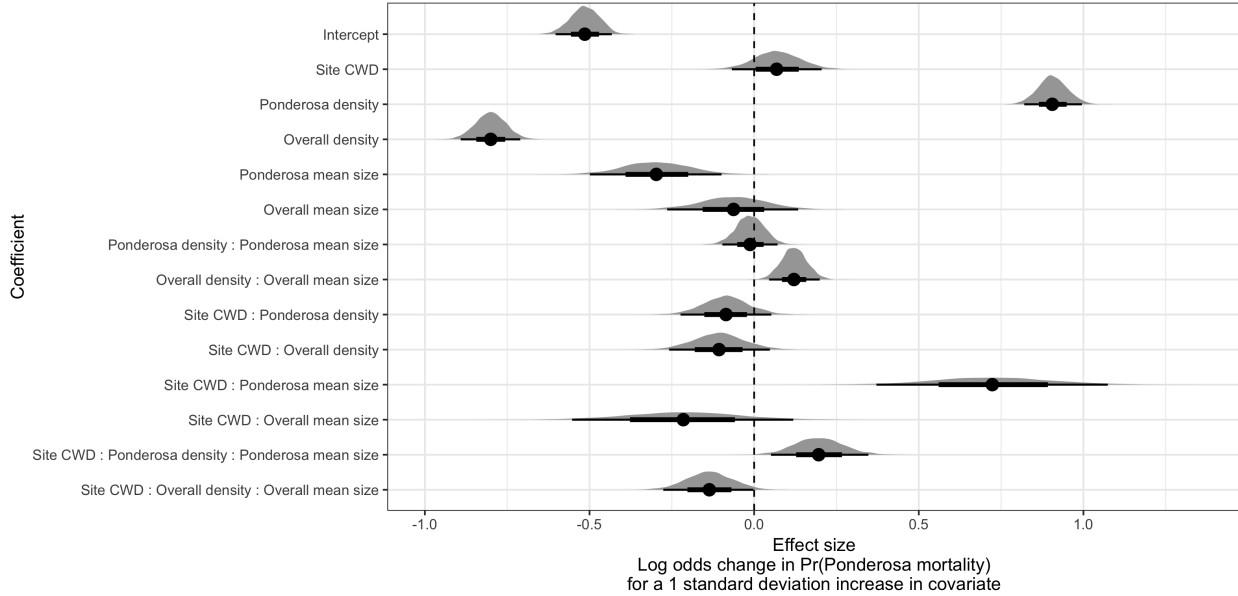


Figure 10: Posterior distributions of effect size from zero-inflated binomial model predicting the probability of ponderosa pine mortality in a 20m x 20m cell given forest structure characteristics of host trees and all trees within the cell, as well as a site-level climatic water deficit. The gray density distribution for each model covariate represents the density of the posterior distribution, the point underneath each density curve represents the median of the estimate, the bold interval surrounding the point estimate represents the 66% credible interval, and the thin interval surrounding the point estimate represents the 95% credible interval.

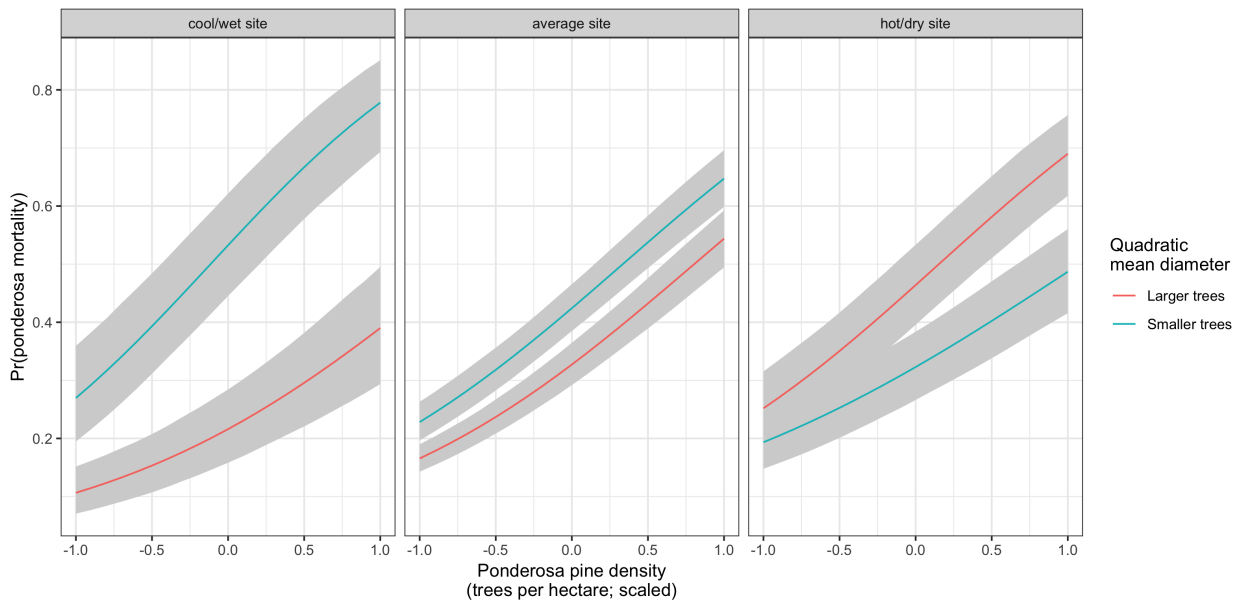


Figure 11: Line version of model results with 95% credible intervals showing primary influence of ponderosa pine structure on the probability of ponderosa pine mortality, and the interaction across climatic water deficit. The “larger trees” line represents the quadratic mean diameter of ponderosa pine 0.7 standard deviations above the mean, and the “smaller trees” line represents the quadratic mean diameter of ponderosa pine 0.7 standard deviations below the mean.

288 **Tree detection**

289 We found that the experimental `lmfx` algorithm with parameter values of `dist2d = 1` and `ws = 2.5` (Roussel  
290 et al. 2019) performed the best across 7 measures of forest structure as measured by Pearson's correlation  
291 with ground data (Table 2).

Table 3: Correlation and differences between the best performing tree detection algorithm (`lmfx` with `dist2d = 1` and `ws = 2.5`) and the ground data. An asterisk next to the correlation or RMSE indicates that this value was within 5% of the value of the best-performing algorithm/parameter set.

| Forest structure metric          | Correlation with ground | RMSE   | Mean error | Median error |
|----------------------------------|-------------------------|--------|------------|--------------|
| height (m); 25th percentile      | 0.16                    | 8.46   | -2.30      | -1.16        |
| height (m); mean                 | 0.29                    | 7.81*  | -3.43      | -2.29        |
| height (m); 75th percentile      | 0.35                    | 10.33* | -4.85      | -3.98        |
| dist to 1st nearest neighbor (m) | 0.55*                   | 1.16*  | 0.13       | 0.26         |
| dist to 2nd nearest neighbor (m) | 0.61*                   | 1.70*  | 0.08       | 0.12         |
| dist to 3rd nearest neighbor (m) | 0.50                    | 2.29   | 0.17       | 0.19         |
| total tree count                 | 0.67*                   | 8.68*  | 0.37       | 2.00         |
| count of trees > 15m             | 0.43                    | 7.38   | 1.18       | 0.00         |
| count of trees < 15m             | 0.58                    | 8.42   | -0.66      | 2.00         |

292 **Effect of local structure and regional climate on western pine beetle severity**

293 We detected no main effect of climatic water deficit on the probability of ponderosa pine mortality within  
294 each 20m x 20m cell.

295 We found a strong main effect of ponderosa pine local density, accounting for quadratic mean diameter of  
296 ponderosa pine, with greater density increasing the probability of ponderosa pine mortality. Conversely,  
297 we found a generally negative effect of quadratic mean diameter of ponderosa pine on the probability of  
298 ponderosa mortality, suggesting that the western pine beetle attacked smaller trees, on average. There was a  
299 strong positive interaction between the climatic water deficit and ponderosa pine quadratic mean diameter,  
300 such that larger trees were more likely to increase the probability of ponderosa mortality in hotter, drier sites.

301 We found negative main effects of overall tree density and overall quadratic mean diameter. There was a  
302 positive interaction between these variables, such that denser stands with larger trees did lead to greater  
303 ponderosa pine mortality.

304 **Spatial effects**

305 We were able to calculate the length scale of the spatial autocorrelation in the probability of ponderosa  
306 pine mortality at each site, accounting for forest structure and environmental factors. By fitting a separate  
307 approximate Gaussian process for each site on the interacting variables of the x- and y- position, we measured  
308 the spatial covariance inherent in the data, accounting for other factors. ## Discussion

309 **Closer spacing between potential host trees facilitates dispersal**

310 If this drives mortality patterns, then we'd expect the local density of ponderosa pine trees, accounting for  
311 other variables, to have a strong positive effect.

312 **Host preference for large trees**

313 If this drives mortality patterns, then we'd expect the quadratic mean diameter of ponderosa pine trees,  
314 accounting for other variables, to have a strong positive effect.

315 **Denser forests augment pheromone communication**

316 If this drives mortality patterns, then we'd expect the local density of all trees, accounting for other variables,  
317 to have a strong positive effect.

318 **Tree crowding leads to greater average water stress per tree**

319 If this drives mortality patterns, then we'd expect the quadratic mean dimater of all trees, accounting for  
320 other factors, to have a strong positive effect.

321 **Interaction between host density and host size**

322 A positive coefficient would indicate a combined effect of WPB preference for large trees and nearby host  
323 availability.

324 **Interaction between all tree density and all tree size**

325 A positive coefficient would indicate a combined effect of tree crowding and pheromone communication  
326 enhancement.

327 **Implications of forest structure/regional climate interactions**

328 We found that the probability of ponderosa pine mortality generally increased with local host availability  
329 (host density), but also interacted with both host size and regional climate such that the role of tree size  
330 became increasingly important in more climatically extreme sites. A smaller average tree size led to a lower  
331 probability of ponderosa mortality in cool/wet sites and a larger average tree size led to a greater probability  
332 of ponderosa mortality in hot/dry sites. These mortality patterns highlight a possible distinction in behavior  
333 between the recent western bark beetle activity across the gradient of climatic water deficit. Even in the most  
334 highly impacted forest stands (because our study sites were selected conditional on there being high levels of  
335 western pine beetle activity), there is still a detectable effect of tree size such that the smaller (presumably  
336 weaker) trees are getting killed in cooler/wetter sites, and the larger (presumably more well-defended) trees  
337 are getting killed more in the hotter/drier sites. So while mortality is high everywhere, there does appear to  
338 be a difference in the beetle choosiness across the climatic water deficit gradient.

339 **Similarities and differences with Fettig et al. (2019)**

340 Fettig et al. (2019) found positive relationship between number of trees killed and: total number of trees,  
341 total basal area, stand density index.  
342 Fettig et al. (2019) found negative relationship between the proportion of trees killed and: total number of  
343 trees, stand density index.  
344 Hayes et al. (2009) and Fettig et al. (2019) found measures of host availability explained less variation in  
345 mortality than measures of stand density.  
346 Negrón et al. (2009) reported positive association of probability of ponderosa pine mortality and tree density  
347 during a drought in Arizona.  
348 Effect of competition may be masked because drought was so extreme Fettig et al. (2019); Floyd et al.  
349 (2009), which is perhaps why we saw a counter-intuitive signal of increasing total basal area leading to lower  
350 probability of ponderosa pine mortality.

351 **Broader context around field plots**

352 We surveyed 9 square kilometers of forest representing ~450,000 trees along a broad gradient. Site selection  
353 and small plot size can influence inference. For instance, Fettig et al. (2019) reported statistically undetectable  
354 differences in overall mortality in their plot network across 4 national forests. By expanding the hectarage  
355 surveyed by a factor of 200, we detected dramatic differences in overall mortality.

356 This is about more than sample size (though that helps). This is also about capturing the local disturbance  
357 phenomenon.

358 **Implications for future forest structure**

359 We have demonstrated that forest structure (local host density and size) affected the cumulative severity  
360 of the western pine beetle in the Sierra Nevada in the 2012 to 2015 drought and its aftermath. Clearly,  
361 this forest insect disturbance has reciprically impacted the forest structure, with uncertain consequences for  
362 long-term forest dynamics.

363 Small trees are getting killed in cooler/wetter sites, larger trees getting killed in hotter/drier sites. Perhaps  
364 the cooler/wetter sites are resisting even this massive disturbance event?

365 **Spatial effect**

366 The western pine beetle is known to exhibit strong aggregation and anti-aggregation behavior arising from  
367 its pheromone communication, and thus it is likely that the measured spatial covariance in this study is  
368 attributable in part to the magnitude of this effect at each site.

369 Some studies have suggested that “outbreak” conditions are distinguishable by clustered tree mortality, but  
370 this is perhaps challenging to tease apart (Raffa et al. 2008). Our modeling framework allows for a joint  
371 estimation of the effects of forest structure, environmental condition, and the spatial effect. This framework  
372 would be enhanced with confidence in individual tree level data, and a lot of it, along with a strong gradient  
373 of environmental conditions and forest structure.

374 We won’t interpret this measure of contagion, because the uncertainties in this particular study are too great  
375 (tree detection, species classification, dead trees all assumed to be WPB hosts, didn’t account for topographic  
376 effects which could also manifest as part of this spatial covariance process). We do suggest that this could be  
377 a meaningful and quantifiable means of assessing bark beetle “stage of outbreak”.

378 **Future spatial directions (will cut this; here for now so I can write it down elsewhere)**

379 Perhaps could also compare relative effect of individual tree spacing (Voronoi polygon area) with the length  
380 scale parameter at a certain site to get at a similar question. A big voronoi polygon area effect and a short  
381 covariance kernel tells us that it’s a water stress effect– a crowded tree gets attacked regardless of whether  
382 nearby trees were attacked. A small voronoi polygon area effect and a long covariance kernel tells us that the  
383 mortality is patterned more based on there being spillover from nearby attacked neighbors instead of how

384 crowded any given tree is. I expect we might see different relative magnitudes of voronoi polygon area and  
385 covariance kerenel effects depending on CWD.

386 **Important considerations**

387 Cumulative effect of elevated insect activity, as mortality was spread out over 5 years and we surveyed at the  
388 end. All the detected dead trees were considered ponderosa pine– we know this is wrong. Only about 3 out  
389 of 4 dead trees in Fettig et al. (2019) were ponderosa.

390 **Room for improvement**

- 391 • Better geometry by using higher overlap, more spatially resolved images.
- 392 • Better image classification and scalability by using instrumentation having spectral overlap with more  
393 widely deployed instrumentation (e.g., Landsat).
- 394 • Better tree detection using machine learning approaches
- 395 • Our live/dead classifier works pretty well.
- 396 • Our species classifier could improve. Perhaps also using machine learning approaches.

397 (Seidl et al. 2015) (Preisler et al. 2017)

398 **References**

- 399 Baldwin, B. G., A. H. Thornhill, W. A. Freyman, D. D. Ackerly, M. M. Kling, N. Morueta-Holme, and B. D.  
400 Mishler. 2017. Species richness and endemism in the native flora of California. American Journal of Botany  
401 104:487–501.
- 402 Brooks, S. P., and A. Gelman. 1998. General Methods for Monitoring Convergence of Iterative Simulations.  
403 Journal of Computational and Graphical Statistics 7:434.
- 404 Bürkner, P.-C. 2017. **Brms** : An *R* Package for Bayesian Multilevel Models Using *Stan*. Journal of Statistical  
405 Software 80.
- 406 Clevers, J., and A. Gitelson. 2013. Remote estimation of crop and grass chlorophyll and nitrogen content using  
407 red-edge bands on Sentinel-2 and -3. International Journal of Applied Earth Observation and Geoinformation  
408 23:344–351.
- 409 Coops, N. C., M. Johnson, M. A. Wulder, and J. C. White. 2006. Assessment of QuickBird high spatial  
410 resolution imagery to detect red attack damage due to mountain pine beetle infestation. Remote Sensing of

- 411 Environment 103:67–80.
- 412 DJI. 2015a. Zenmuse X3 - Creativity Unleashed. <https://www.dji.com/zenmuse-x3/info>.
- 413 DJI. 2015b. DJI - The World Leader in Camera Drones/Quadcopters for Aerial Photography. <https://www.dji.com/matrice100/info>.
- 414
- 415 Easy, D. M. 2018. Map Pilot for DJI. <https://itunes.apple.com/us/app/map-pilot-for-dji/id1014765000?mt=8>.
- 416 Eysn, L., M. Hollaus, E. Lindberg, F. Berger, J.-M. Monnet, M. Dalponte, M. Kobal, M. Pellegrini, E.
- 417 Lingua, D. Mongus, and N. Pfeifer. 2015. A Benchmark of Lidar-Based Single Tree Detection Methods Using
- 418 Heterogeneous Forest Data from the Alpine Space. *Forests* 6:1721–1747.
- 419 Farr, T. G., P. A. Rosen, E. Caro, R. Crippen, R. Duren, S. Hensley, M. Kobrick, M. Paller, E. Rodriguez, L.
- 420 Roth, D. Seal, S. Shaffer, J. Shimada, J. Umland, M. Werner, M. Oskin, D. Burbank, and D. Alsdorf. 2007.
- 421 The Shuttle Radar Topography Mission. *Reviews of Geophysics* 45.
- 422 Fettig, C. J. 2012. Chapter 2: Forest health and bark beetles. *in* Managing Sierra Nevada Forests. PSW-
- 423 GTR-237. USDA Forest Service.
- 424 Fettig, C. J., L. A. Mortenson, B. M. Bulaon, and P. B. Foulk. 2019. Tree mortality following drought in the
- 425 central and southern Sierra Nevada, California, U.S. *Forest Ecology and Management* 432:164–178.
- 426 Flint, L. E., A. L. Flint, J. H. Thorne, and R. Boynton. 2013. Fine-scale hydrologic modeling for regional land-
- 427 scape applications: The California Basin Characterization Model development and performance. *Ecological*
- 428 *Processes* 2:25.
- 429 Floyd, M. L., M. Clifford, N. S. Cobb, D. Hanna, R. Delph, P. Ford, and D. Turner. 2009. Relationship of
- 430 stand characteristics to drought-induced mortality in three Southwestern piñonJuniper woodlands. *Ecological*
- 431 *Applications* 19:1223–1230.
- 432 Gabry, J., D. Simpson, A. Vehtari, M. Betancourt, and A. Gelman. 2019. Visualization in Bayesian workflow.
- 433 *Journal of the Royal Statistical Society: Series A (Statistics in Society)* 182:389–402.
- 434 Gitelson, A., and M. N. Merzlyak. 1994. Spectral Reflectance Changes Associated with Autumn Senescence
- 435 of *Aesculus hippocastanum* L. and *Acer platanoides* L. Leaves. Spectral Features and Relation to Chlorophyll
- 436 Estimation. *Journal of Plant Physiology* 143:286–292.
- 437 Hayes, C. J., C. J. Fettig, and L. D. Merrill. 2009. Evaluation of Multiple Funnel Traps and Stand
- 438 Characteristics for Estimating Western Pine Beetle-Caused Tree Mortality. *Journal of Economic Entomology*

- <sup>439</sup> 102:2170–2182.
- <sup>440</sup> Hijmans, R. J., J. van Etten, M. Sumner, J. Cheng, A. Bevan, R. Bivand, L. Busetto, M. Canty, D. Forrest,  
<sup>441</sup> A. Ghosh, D. Goliche, J. Gray, J. A. Greenberg, P. Hiemstra, I. for M. A. Geosciences, C. Karney, M.  
<sup>442</sup> Mattiuzzi, S. Mosher, J. Nowosad, E. Pebesma, O. P. Lamigueiro, E. B. Racine, B. Rowlingson, A. Shortridge,  
<sup>443</sup> B. Venables, and R. Wueest. 2019. *Raster: Geographic Data Analysis and Modeling*.
- <sup>444</sup> Hunziker, P. 2017. *Velox: Fast Raster Manipulation and Extraction*.
- <sup>445</sup> Jakubowski, M. K., W. Li, Q. Guo, and M. Kelly. 2013. Delineating Individual Trees from Lidar Data: A  
<sup>446</sup> Comparison of Vector- and Raster-based Segmentation Approaches. *Remote Sensing* 5:4163–4186.
- <sup>447</sup> Kane, V. R., M. P. North, J. A. Lutz, D. J. Churchill, S. L. Roberts, D. F. Smith, R. J. McGaughey, J. T.  
<sup>448</sup> Kane, and M. L. Brooks. 2014. Assessing fire effects on forest spatial structure using a fusion of Landsat and  
<sup>449</sup> airborne LiDAR data in Yosemite National Park. *Remote Sensing of Environment* 151:89–101.
- <sup>450</sup> Kuhn, M. 2008. Building Predictive Models in R Using the caret Package. *Journal of Statistical Software*  
<sup>451</sup> 28:1–26.
- <sup>452</sup> Larson, A. J., and D. Churchill. 2012. Tree spatial patterns in fire-frequent forests of western North America,  
<sup>453</sup> including mechanisms of pattern formation and implications for designing fuel reduction and restoration  
<sup>454</sup> treatments. *Forest Ecology and Management* 267:74–92.
- <sup>455</sup> Li, W., Q. Guo, M. K. Jakubowski, and M. Kelly. 2012. A New Method for Segmenting Individual Trees  
<sup>456</sup> from the Lidar Point Cloud. *Photogrammetric Engineering & Remote Sensing* 78:75–84.
- <sup>457</sup> Meyer, F., and S. Beucher. 1990. Morphological segmentation. *Journal of Visual Communication and Image  
Representation* 1:21–46.
- <sup>459</sup> Micasense. 2015. MicaSense. <https://support.micasense.com/hc/en-us/articles/215261448-RedEdge-User-Manual-PDF-Download>
- <sup>460</sup> Millar, C. I., and N. L. Stephenson. 2015. Temperate forest health in an era of emerging megadisturbance.  
<sup>461</sup> *Science* 349:823–826.
- <sup>462</sup> Morris, J. L., S. Cottrell, C. J. Fettig, W. D. Hansen, R. L. Sherriff, V. A. Carter, J. L. Clear, J. Clement, R.  
<sup>463</sup> J. DeRose, J. A. Hicke, P. E. Higuera, K. M. Mattor, A. W. R. Seddon, H. T. Seppä, J. D. Stednick, and S.  
<sup>464</sup> J. Seybold. 2017. Managing bark beetle impacts on ecosystems and society: Priority questions to motivate  
<sup>465</sup> future research. *Journal of Applied Ecology* 54:750–760.
- <sup>466</sup> Negrón, J. F., J. D. McMillin, J. A. Anhold, and D. Coulson. 2009. Bark beetle-caused mortality in a

- 467 drought-affected ponderosa pine landscape in Arizona, USA. Forest Ecology and Management 257:1353–1362.
- 468 North, M. P., S. L. Stephens, B. M. Collins, J. K. Agee, G. Aplet, J. F. Franklin, and P. Z. Fule. 2015.
- 469 Reform forest fire management. Science 349:1280–1281.
- 470 Pau, G., F. Fuchs, O. Sklyar, M. Boutros, and W. Huber. 2010. EBImagean R package for image processing  
471 with applications to cellular phenotypes. Bioinformatics 26:979–981.
- 472 Pebesma, E., R. Bivand, E. Racine, M. Sumner, I. Cook, T. Keitt, R. Lovelace, H. Wickham, J. Ooms, K.  
473 Müller, and T. L. Pedersen. 2019. Sf: Simple Features for R.
- 474 Plowright, A. 2018. ForestTools: Analyzing Remotely Sensed Forest Data.
- 475 Popescu, S. C., and R. H. Wynne. 2004. Seeing the Trees in the Forest: Using Lidar and Multispectral Data  
476 Fusion with Local Filtering and Variable Window Size for Estimating Tree Height. PHOTOGGRAMMETRIC  
477 ENGINEERING:16.
- 478 Preisler, H. K., N. E. Grulke, Z. Heath, and S. L. Smith. 2017. Analysis and out-year forecast of beetle,  
479 borer, and drought-induced tree mortality in California. Forest Ecology and Management. 399: 166–178  
480 399:166–178.
- 481 R Core Team. 2018. R: A Language and Environment for Statistical Computing. R Foundation for Statistical  
482 Computing, Vienna, Austria.
- 483 Raffa, K. F., B. H. Aukema, B. J. Bentz, A. L. Carroll, J. A. Hicke, M. G. Turner, and W. H. Romme. 2008.  
484 Cross-scale Drivers of Natural Disturbances Prone to Anthropogenic Amplification: The Dynamics of Bark  
485 Beetle Eruptions. BioScience 58:501–517.
- 486 Raffa, K. F., J.-C. Grégoire, and B. Staffan Lindgren. 2015. Natural History and Ecology of Bark Beetles.  
487 Pages 1–40 in Bark Beetles. Elsevier.
- 488 Rouse, W., R. H. Haas, W. Deering, and J. A. Schell. 1973. MONITORING THE VERNAL ADVANCEMENT  
489 AND RETROGRADATION (GREEN WAVE EFFECT) OF NATURAL VEGETATION. Type II Report,  
490 Goddard Space Flight Center, Greenbelt, MD, USA.
- 491 Roussel, J.-R. 2019. lidRplugins: Extra functions and algorithms for lidR package.
- 492 Roussel, J.-R., D. A. (. the documentation), F. D. B. (. bugs and improved catalog features), and A. S. M. (.  
493 lassnags). 2019. lidR: Airborne LiDAR Data Manipulation and Visualization for Forestry Applications.
- 494 Seidl, R., J. Müller, T. Hothorn, C. Bässler, M. Heurich, and M. Kautz. 2015. Small beetle, large-scale  
495 drivers: How regional and landscape factors affect outbreaks of the European spruce bark beetle. The Journal

- 496 of applied ecology 53:530–540.
- 497 Shiklomanov, A. N., B. A. Bradley, K. M. Dahlin, A. M. Fox, C. M. Gough, F. M. Hoffman, E. M. Middleton,  
498 S. P. Serbin, L. Smallman, and W. K. Smith. 2019. Enhancing global change experiments through integration  
499 of remote-sensing techniques. *Frontiers in Ecology and the Environment* 0.
- 500 Shin, P., T. Sankey, M. Moore, and A. Thode. 2018. Evaluating Unmanned Aerial Vehicle Images for  
501 Estimating Forest Canopy Fuels in a Ponderosa Pine Stand. *Remote Sensing* 10:1266.
- 502 Stephenson, N. 1998. Actual evapotranspiration and deficit: Biologically meaningful correlates of vegetation  
503 distribution across spatial scales. *Journal of Biogeography* 25:855–870.
- 504 Stephenson, N. L., A. J. Das, N. J. Ampersee, and B. M. Bulaon. 2019. Which trees die during drought?  
505 The key role of insect host-tree selection. *Journal of Ecology*:75.
- 506 USDAFS. 2019, February 11. Press Release: Survey finds 18 million trees died in California in 2018.  
507 [https://www.fs.usda.gov/Internet/FSE\\_DOCUMENTS/FSEPRD609321.pdf](https://www.fs.usda.gov/Internet/FSE_DOCUMENTS/FSEPRD609321.pdf).
- 508 Vega, C., A. Hamrouni, S. El Mokhtari, J. Morel, J. Bock, J. P. Renaud, M. Bouvier, and S. Durrieu. 2014.  
509 PTrees: A point-based approach to forest tree extraction from lidar data. *International Journal of Applied  
510 Earth Observation and Geoinformation* 33:98–108.
- 511 Young, D. J. N., J. T. Stevens, J. M. Earles, J. Moore, A. Ellis, A. L. Jirka, and A. M. Latimer. 2017.  
512 Long-term climate and competition explain forest mortality patterns under extreme drought. *Ecology Letters*  
513 20:78–86.
- 514 Zhang, W., J. Qi, P. Wan, H. Wang, D. Xie, X. Wang, and G. Yan. 2016. An Easy-to-Use Airborne LiDAR  
515 Data Filtering Method Based on Cloth Simulation. *Remote Sensing* 8:501.